Int J Earth Sci (Geol Rundsch) (2016) 105:2149–2160
DOI 10.1007/s00531-016-1294-3

ORIGINAL PAPER

The M_w6.7 12 October 2013 western Hellenic Arc main shock and its aftershock sequence: implications for the slab properties

Eleftheria Papadimitriou[1] · Vassilis Karakostas[1] · Maria Mesimeri[1] · Filippos Vallianatos[2]

Received: 27 August 2015 / Accepted: 31 December 2015 / Published online: 20 January 2016
© Springer-Verlag Berlin Heidelberg 2016

Abstract The 12 October 2013 M_w6.7 earthquake offshore Crete Island is one of the few strong earthquakes to have occurred in the last few decades in the southwestern part of the Hellenic subduction zone (HSZ), providing the opportunity to evaluate characteristics of the descending slab. The HSZ has experienced several strong ($M \geq 7.0$) earthquakes in historical times with the largest one being the 365 AD, $M_w = 8.4$ earthquake, the largest known ever occurred in the Mediterranean region. The 2013 main shock occurred in close proximity with the 365 event, on an interplate thrust fault at a depth of 26 km, onto the coupled part of the overriding and descending plates. GCMT solution shows a slightly oblique (rake = 130°) thrust faulting with downdip compression on a nearly horizontal (dip = 3°) northeast-dipping fault plane with strike (340°) parallel to the subduction front, with the compression axis being oriented in the direction of plate convergence. The subduction interface can be more clearly resolved with the integration of aftershock locations and CMT solution. For this scope, the aftershocks were relocated after obtaining a v_p/v_s ratio equal to 1.76, a one-dimensional velocity model and time delays that approximate the velocity structure of the study area, and the employment of double-difference technique for both phase pick data and cross-correlation differential times. The first-day relocated seismicity, alike aftershocks in the first 2 months, shows activation of an area at the upper part of the descending slab, with most activity being concentrated between 13 and 27 km, where the main shock is also encompassed. Aftershocks are rare near to the main shock, implying homogeneous slip on a large patch of the rupture plane. Based on the aftershock distribution, the size of the activated area estimated is about 24 km long and 17 km wide. Coulomb stress changes resolved for transpressive motion reveal negligible off-fault aftershock triggering, evidencing a comparatively stable regime in the downdip part of the slab or different fault mechanism.

Keywords 2013 Crete earthquake · Aftershock relocation · Hellenic subduction zone

✉ Eleftheria Papadimitriou
ritsa@geo.auth.gr

Vassilis Karakostas
vkarak@geo.auth.gr

Maria Mesimeri
mmesimer@geo.auth.gr

Filippos Vallianatos
fvallian@chania.teicrete.gr

[1] Geophysics Department, Aristotle University of Thessaloniki, 54124 Thessaloníki, Greece

[2] Laboratory of Geophysics and Seismology, Technological Educational Institute of Crete, Chania, Greece

Introduction

The 2013 M_w6.7 Crete earthquake sequence is associated with a fault segment of the almost rectilinear southwestern part of the Hellenic subduction zone (HSZ) (Fig. 1). The oceanic plate of eastern Mediterranean, the front part of the northward moving African lithospheric plate, is subducting northeasterly beneath the Aegean microplate, the southern portion of Eurasian lithospheric plate in this area (Papazachos and Comninakis 1971; Papazachos et al. 1998, 2000), also supported and confirmed by geodetic data analysis (e.g., McClusky et al. 2000; Reilinger et al. 2010). The Aegean is fast moving (~33 mm/year) to the southwest overriding the oceanic plate, with the African moving almost to the north at a much smaller rate (~5 mm/

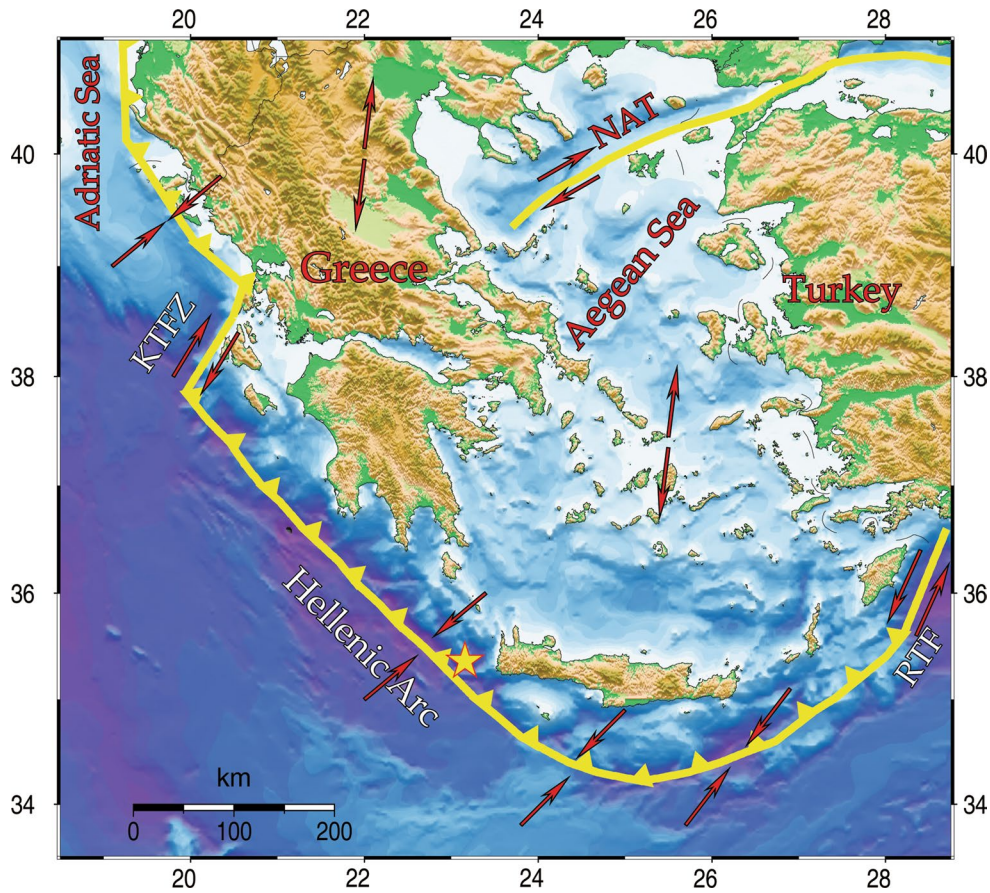

Fig. 1 Aegean and surrounding areas with the major active boundaries and the sense of relative motions. The 2013 main shock epicenter is shown by the asterisk. *KTFZ* Kefalonia transform fault zone, *RTF* Rodos transform fault, *NAT* North Aegean trough

year) at the convergence area (Ganas and Parsons 2009). The Hellenic Arc is laterally bounded by subduction-transform edge propagators (STEP), kinks in the plate boundary that are ongoing tearing of oceanic lithosphere near the horizontal terminations of subduction trenches (Govers and Wortel 2005), the dextral Kefalonia transform zone in the west (Scordilis et al. 1985) and the sinistral Rodos Fault in the east (Papazachos and Papazachou 2003). The western part of the Hellenic Arc accommodated the great 365 AD M_w8.4 earthquake (Papazachos and Papazachou 2003; Papadimitriou and Karakostas 2008), the largest event ever reported in the Mediterranean area, followed by a tremendous tsunami that affected the entire eastern Mediterranean area from the Dinaric up to Palestine coasts. Only one more earthquake exceeding $M \sim 8.0$ was reported for this area (1303 M8 near Rodos Island, at the eastern edge of the HSZ), implying that the maximum possible earthquake for the region is the one observed in 365 AD.

$M \sim 7.0$ earthquakes are rare in the entire subduction zone, less than expected from regional plate motions rates. The seismic coupling coefficient at this plate boundary has been estimated at approximately 10 % or less (Papadimitriou and Karakostas 2005). During the instrumental era, five intermediate depth earthquakes of $7.0 \leq M \leq 7.5$ and five shallow ones with $7.0 \leq M \leq 7.2$ were recorded (see "Appendix"). The 2013 sequence, therefore, provides an exceptional opportunity to seeking for details on the rupture geometry and aftershock behavior across the plate interface, at the location of the 365 AD event, the inferred fault trace of which is denoted by the thick red line in Fig. 2. The rupture model of this great earthquake was constructed by Papadimitriou and Karakostas (2008) who assumed an elastic medium, calculated the theoretical surface displacement and compared the latter with the observed surface deformation (from Pirazzoli et al. 1996). The resulted rupture model implies a thrust fault with a length of 160 km and a seismic moment of 5.7×10^{28} dyn cm, an average slip of 8.9 m and a corresponding moment magnitude equal to 8.4.

The 2013 earthquake is the largest that occurred in the last four decades along the western part of the Hellenic subduction zone and caused light damage in western Crete. The rupture dimensions of subduction events are in general more difficult to estimate due to their position in relation to seismological networks geometry. Analysis of the aftershock sequence allowed the investigation of this rupture characteristics as in detail as possible, consequently shedding more light in the geometry of the descending slab. The main shock occurred on a thrust fault at a depth of 26 km, inside the coupled part of the subducted oceanic crust, with the compression axis being oriented in the direction of

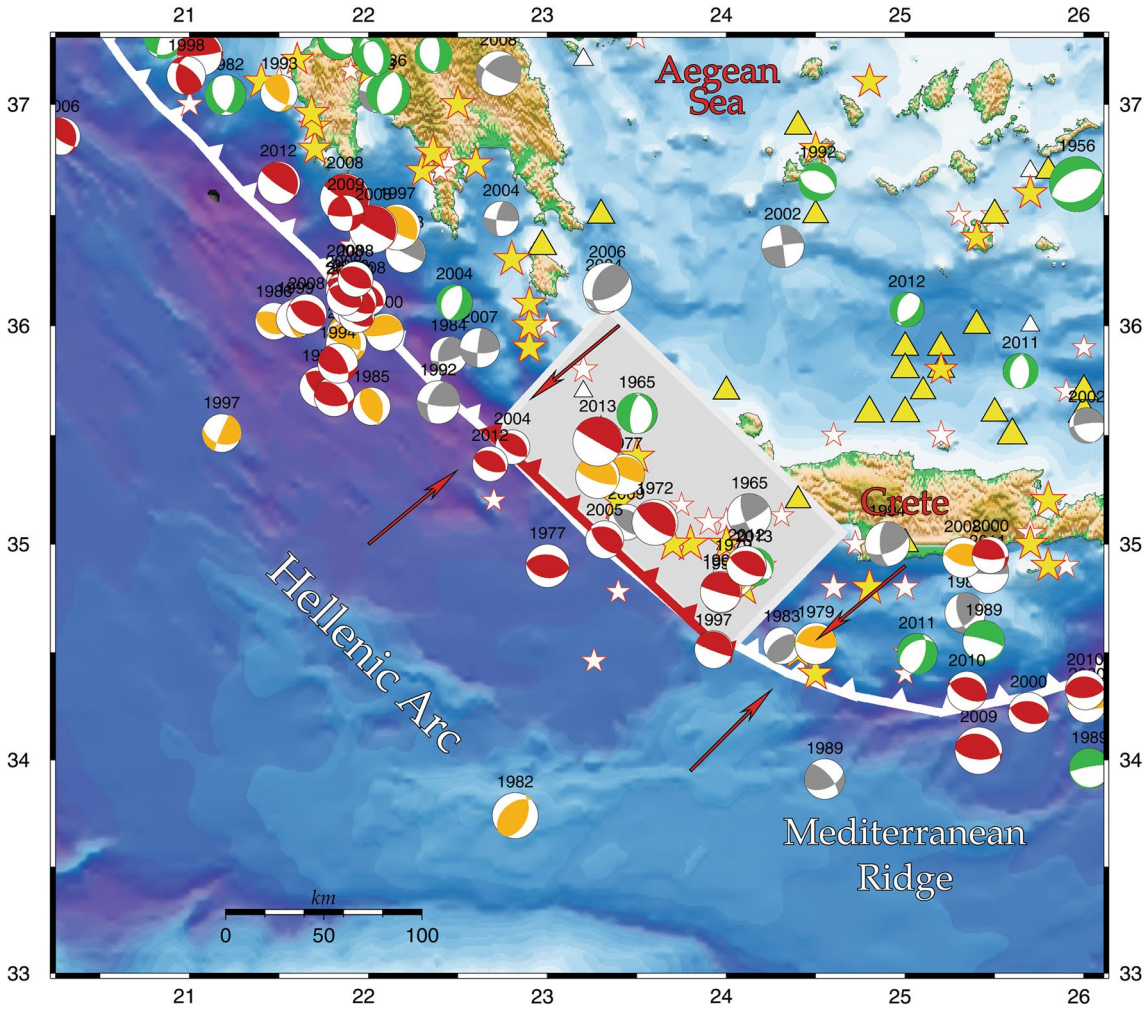

Fig. 2 Historical seismicity in the study area with *stars* (bigger for $M \geq 6.5$ and smaller for $M \geq 6.0$) representing subduction and crustal earthquakes (shallower than 50 km) and *triangles* (again, bigger for $M \geq 6.5$ and smaller for $M \geq 6.0$, respectively) intermediate depth (deeper than 50 km) earthquakes. The available fault plane solutions are depicted as lower hemisphere equal area projections (compression quadrants are in red for thrust faulting, orange for transpression, *green* for normal faulting, in depths less than 50 km, and *light gray* for intermediate depth events). The surface projection of the great 365 AD rupture area is shown by the *rectangle*

plate convergence (strike = 211°, plunge = 42°) as it is evidenced from the GCMT solution (http://www.ldeo.columbia.edu/~gcmt/) (strike = 339°, dip = 3°, rake = 130°). The relocated seismicity shows activation of the lower part of the descending slab in depths between 13 and 27 km, where the main shock is also encompassed. The aftershock distribution reveals that the activated area is 24 km long and 17 km wide, as shown later. Cross-sectional views of the relocated seismicity evidenced the extent of the main rupture, along with a few off-fault aftershocks.

Historical seismicity and faulting type

The latest $M \geq 6.0$ thrust faulting earthquake to occur prior to 2013 main shock had an M_w6.3 on 4 May 1972 southwards and just offshore the southwestern corner of Crete Island inside the rupture area of the great 365 AD event, the surface projection of which is shown as a rectangle in Fig. 2. This was associated with thrust faulting (strike: 309°, dip: 18°, rake: 89°) exhibiting maximum compression almost perpendicular to the subduction direction (Kiratzi and Langston 1989), as was the case for most other events occurred in the same region. It was at a distance of almost one fault length, corresponding to this magnitude order (M ~ 6.0–6.5) earthquakes, meaning to an adjacent fault patch, whereas to the northwest the 2008 extremely intense seismic sequence (comprising 3 events of M6.7, M6.1 and M6.0) took place at a longer distance. Nevertheless, the $M \geq 6.5$ events are very few (the largest beach balls in Fig. 2), to account for the deformation anticipated from the plate motion.

Four different styles of faulting are distinguished in the area around the 2013 rupture, mostly exhibiting shortening along the subduction front, either pure thrusting or transpression (red and orange compressional quadrants, respectively). The 2013 main shock exhibited oblique thrusting with fault strike coinciding with the trend of the subduction direction at its epicentral area. The overriding plate is stretched in E–W direction along a broad zone running parallel to the subduction front along the convergence margin and in the forearc area (green compressional quadrants). Farther to the north, the back arc extension is taking place in an N–S direction, resulted from the slab roll back. Intermediate depth earthquakes are associated mostly with strike-slip faulting (gray compression quadrants), with downdip extension expressing slab pull at these depths (e.g., 2006 Kithira earthquake, Nikolintaga et al. 2008).

Aftershocks location

For investigating the spatial aftershock distribution, the earthquake catalog produced by the routine analysis by the Department of Geophysics of the Aristotle University of Thessaloniki was employed. The reason for this selection rests on the availability of raw data, since in addition to the phase data, we have access to the waveforms for original picking, picking corrections and for using them in the cross-correlation procedure. Aiming to create a highly accurate earthquake, catalog data from the stations of the Hellenic Unified Seismic Network were used (HUSN, http://www.gein.noa.gr/en/networks/husn) along with those of the Hellenic Seismological Network of Crete (HSNC, Hloupis et al. 2013).

1-D velocity model

To improve hypocentral determination, an average v_p/v_s ratio was calculated based upon the linearity of Wadati diagrams (Wadati 1933). For a medium of constant velocity, one can write $t_p = t_0 + d/v_p$, $t_s = t_0 + d/v_s$, where t_p and t_s are the P-wave and S-wave travel times, respectively, 'd' is the hypocentral distance, t_0 is the origin time, and v_p and v_s are the P-wave and S-wave speeds, respectively. Combining the above equations, one can obtain $t_s - t_p = (v_p/v_s - 1)\ (t_p - t_0)$, which is the equation of a line with slope $(v_p/v_s - 1)$ and intercept with the abscissa at $t_p = t_0$. The slope of the Wadati line conveys information on the v_p/v_s ratio of the propagating medium, while the intercept with the abscissa yields corrections on the event's origin time. The recordings of 43 earthquakes that occurred in the first 36 h after the main shock with five S-arrivals or more were used. Fitting the $(t_s - t_p)$ versus $(t_p - t_0)$ and setting $t_0 = 0$, for all available pairs, an average v_p/v_s ratio of 1.76 was resulted (Fig. 3). This is quite similar with the value of 1.77 estimated for subcrustal seismicity location only by Hatzfeld et al. (1990), and the 1.75 for western and central Crete and Gavdos Island by Meier et al. (2004). The P-wave velocity model (Table 1) was adopted from Meier et al. (2004).

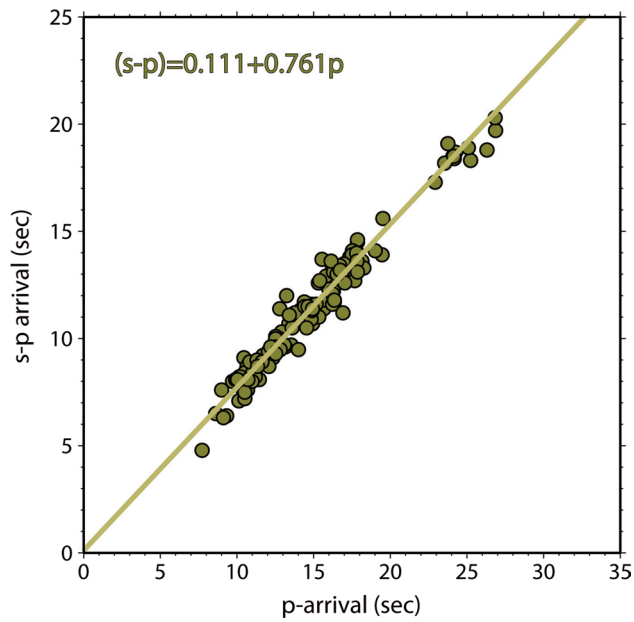

Fig. 3 v_p/v_s ratio for the aftershock sequence resulted from the linear fit of t_p–t_s versus t_p

Table 1 P-wave velocity model used for the relocation, adopted from Meier et al. (2004)

P-wave velocity (km/s)	Depth (km)
4.20	0.0
5.70	1.0
6.30	3.0
6.40	8.0
6.45	12.0
6.50	20.0
6.80	25.0
7.30	30.0
7.90	33.0

Firstly, aftershock location was achieved with the use of the HYPOINVERSE computer program (Klein 2000). For incorporating lateral heterogeneities in the velocity model, station corrections were calculated after repetitive iterations until the changes in their values become negligible (e.g., Karakostas et al. 2014). The resulted locations were used as input to the hypoDD program (Waldhauser and Ellsworth 2000; Waldhauser 2001), and relocation was performed using the catalog data for both P- and S-phases

and application of the conjugate gradients method (LSQR, Paige and Saunders 1982). The recordings were taken from 36 seismological stations at epicentral distances less than 200 km from the main shock epicenter. Since the seismic sequence occurred offshore, the closest stations are at a distance of 50 km and their positions are distributed along the western coast of Crete Island, a typical case for sequences along subduction zones. The origin times of the obtained catalog were used for preparing the waveforms.

Cross-correlation

Differential times of cross-correlation measurements were obtained following the method described by Schaff et al. (2004) and Schaff and Waldhauser (2005) in order to achieve highly accurate locations. For that purpose, the recordings of 28 stations that are in distances up to 200 km were collected. Waveforms with 120-s duration having sampling rate 100 samples/sec were selected, based on an event catalog derived using hypoDD. In these waveforms, a band-pass filter (1.5–15 Hz) was performed as the instruments are reliable in this frequency range. An important parameter in the correlation process is the choice of the window length. It has been shown that long window lengths give lower residuals and sharper locations (Schaff et al. 2004). On the other hand, the correlation coefficient (CC) is decreasing with increasing window lengths. After conducting several tests with different window lengths, we chose the 2-s window length for both P- and S-waves. The searched over lags were ±1 s. In this procedure, only the manually picked P- and S-phases were considered without calculating theoretical travel times where manually picked phases were not available. From all the calculated cross-correlation measurements, only those with CC ≥ 0.7 were kept, resulting in 1733 event pairs with 2569 P- and 1627 S-phases. An example of similar waveforms from different earthquakes recorded at station IMMV is shown in Fig. 4. The correlation coefficient of the waveform with id number 34 (shown in the first row in Fig. 4) is higher than or equal to 0.8 correlated with each one of the waveforms in the next rows.

The double-difference method was used for relocating the events of the sequence after combining the cross-correlation differential times with these from phase picking catalog. A total of 25 iterations were performed with proper weighting of both data sets in order to achieve precise locations. In the first 15 iterations, the cross-correlation data were down-weighted by a factor of 100 in order to allow the location from the catalog data. In the later 10 iterations, the catalog data were down-weighted by a factor of 100 and the locations were based on cross-correlation differential times. The resulted locations (91 events) are highly accurate with a mean rms 10 ms and a mean vertical and horizontal error 20 m. It is worth mentioning that the main shock was located using the catalog data since it was not possible to correlate this event with any others due to its large size, in comparison with its aftershocks.

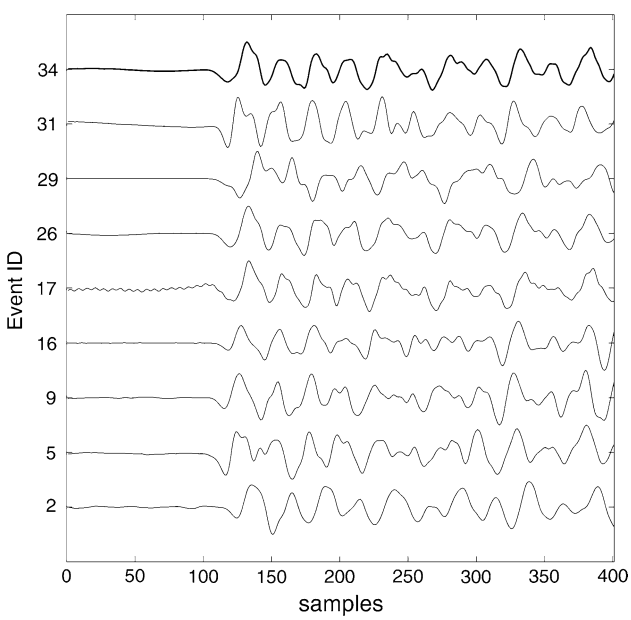

Fig. 4 Example of P-wave trains recorded at station IMMV. All the events are similar to event 34 with correlation coefficient (CC) exceeding 0.8. *X*-axes are in samples (delta = 0.01 s)

Aftershock distribution

The data set includes 91 aftershocks with magnitudes $M \geq 1.7$ that were detected in the first 50 days and relocated as described in the previous section. Their epicentral distribution is shown in Fig. 5, where asterisks represent the first-day activity, which is assumed to reveal the main rupture area (rectangle in Fig. 5). The aftershock activity is confined almost totally inside this area during the 50 days and is extended ~24 km. The main shock is located roughly in the middle of the northwestern part of this region, with very few close aftershocks, implying the location of a roughly homogeneous slip at this part of the rupture area. The maximum magnitude aftershock (M4.0) is quite far from what is expected from Bath's law, and aftershock rate was relatively fast. This pattern of small magnitude aftershock activity implies that the post-seismic deformation is remarkably minor. For the sake of comparison, we have sought the aftershock number of the recent (after 2000) main shocks with $M \geq 6.0$ that occurred in the Greek territory. It revealed that this was the one of two cases out of eleven seismic sequences in this time interval, where there was only one event with $M \geq 4.0$, and about 20 aftershocks with $3.0 \leq M < 4.0$.

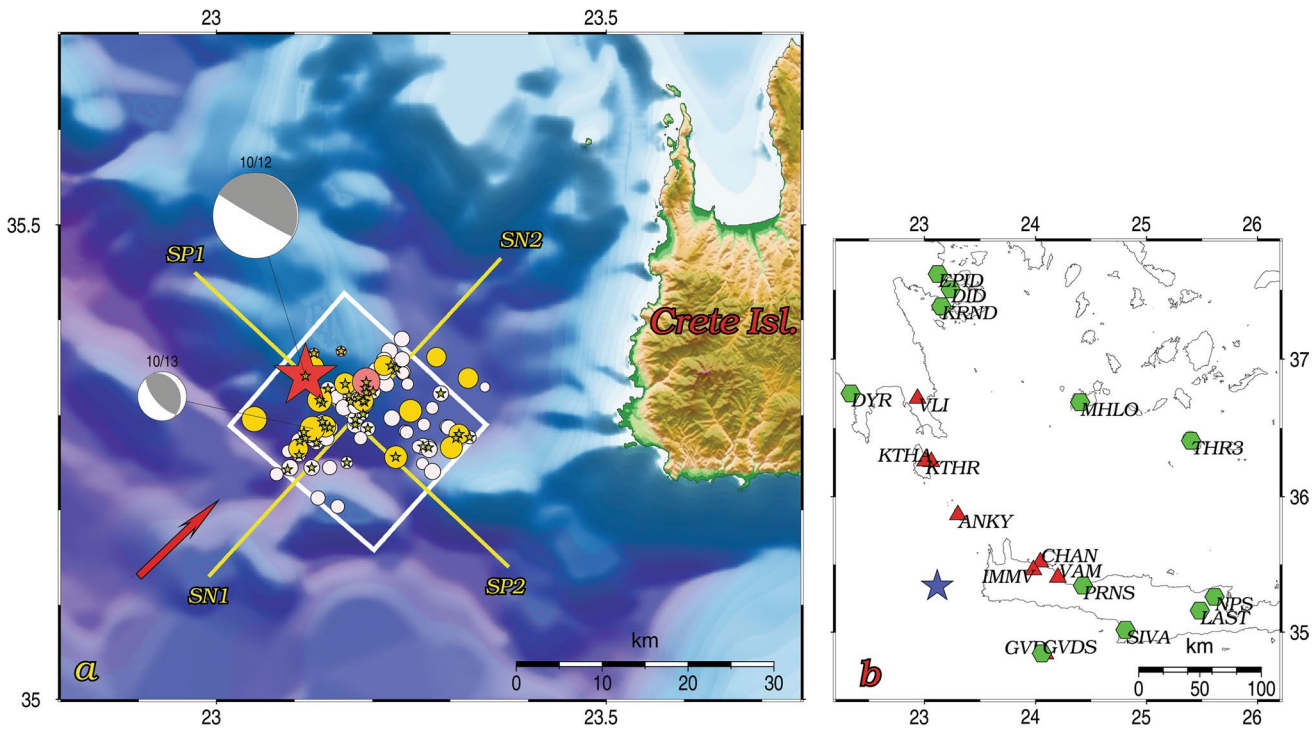

Fig. 5 **a** Relocated main shock epicenter is shown by the *star*, the largest aftershock by the *biggest circle* to the east, and the aftershocks by *circles* with size proportional to their magnitude. The *rectangle* is the surface projection of the inferred fault plane. The positions of the strike normal (*SN1–SN2*) and strike parallel (*SP1–SP2*) cross sections. Fault plane solutions of the main shock and one aftershock are shown as lower hemisphere equal area projections. The *arrow* shows relative plate motion. **b** *Triangles* depict the locations of the stations provided more than one hundred phases used for the relocation, whereas *hexagons* the ones with less phases

The rupture area is estimated to be 24 km long in the NW–SE direction along the subduction front and 17 km wide in the SW–NE direction. The spatial distribution of the relocated aftershocks is in adequate agreement with the one nodal plane of the global centroid moment tensor (GCMT) solution. This solution agrees well with the ones found for adjacent strong events in the recent past (04/05/1972, M_w6.3, strike = 308°, dip = 18°, rake = 90°, Kiratzi and Langston (1989); 29/11/1973, M_w5.8, strike = 283°, dip = 38°, rake = 97°, Papadimitriou (1993); 18/08/1977, M_w5.5, strike = 270°, dip = 12°, rake = 62°, Taymaz et al. (1990); 21/06/1984, M_w6.0, strike = 322°, dip = 16°, rake = 114°, Papadimitriou (1993)), revealing low-angle thrusting and convergence at a direction of ~30°.

Faulting and slab geometry

The relocated main shock at a depth of 26 km seems to have been nucleated at the lower part of the seismogenic layer of the oceanic crust (Fig. 6). The seismogenic layer revealed by the vertical distribution of the precisely located in depth aftershocks is confined in depths between 13 and 27 km (strike parallel cross section). A very gently dipping nodal plane could be inferred, consistent with the GCMT solution for the main shock and one aftershock (available from National Observatory of Athens at http://bbnet.gein.noa.gr/HL/seismicity/moment-tensors). Compression is slightly orthogonal to the aftershock alignment in the cross section and obliquely positioned to the dip direction of the slightly bending oceanic crust at this site.

The location of the main asperity where the main shock is located is defined by a gap in the highly active patches formed by aftershock distribution, evidenced mainly in the strike parallel projection. It is noticeable that aftershocks are lacking further downdip, although it is a stress favored area as it will be shown in the next section. This could be attributed to mechanical properties of the slab at this depth, inhibiting off-fault activity to be triggered. The sectional distribution implies a frictional model for an upper ~13-km stable zone where seismic slip cannot be supported, and an unstable zone in between 13 and 27 km, where strain accumulation and seismic slip take place.

With the purpose to shed more light in the slab geometry, data from the regional network were used for relocating earthquakes that occurred in 2011–2015 at a distance of 40 km either side of the line AB, which is traced perpendicular to the convergence front at the site of the seismic sequence. Relocation was performed with HypoDD

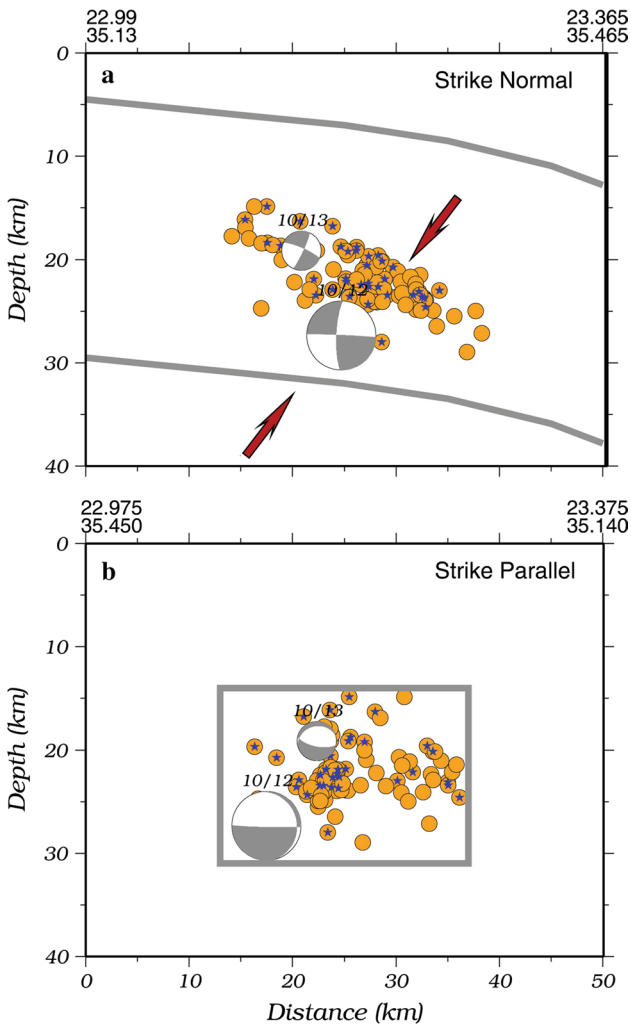

Fig. 6 Cross sections of the seismicity shown in Fig. 5. **a** Strike normal vertical section (SN1–SN2 in Fig. 5) with the inferred boundaries of the oceanic crust and **b** strike parallel section (SP1–SP2 in Fig. 5) where the *box* denotes the inferred rupture plane

program for this data set, except for a small group located to the southwest due to the small number of earthquakes there, where locations were evaluated with HYPOINVERSE (Fig. 7a). Seismicity is mainly confined between 5 and 30 km, implying a width for the oceanic brittle crust of 25 km. The locations of the 2013 sequence (shown in red in Fig. 7b) occupy the nearest to the convergence part of the active layer, providing evidence that the strong ($M \geq 6.0$) earthquakes can nucleate at this site of the convergence front. This agrees with the locations of these shocks along with the modeled rupture of the 365 AD large earthquake (Fig. 2). Intermediate depth seismicity, although sparse, consistently continues downdip up to focal depths of 100 km, implying a subduction angle of ~30°, in adequate agreement with Papazachos et al. (2000).

Stress changes

For the calculation of static stress changes due to the coseismic slip of the main shock, the main rupture is approximated as a planar surface imbedded into the half space and dipping to northeast, with dimensions of 24 km in length and 17 km in width, defined based on the aftershock 3-D distribution (Fig. 6). Although in this approximation the aftershock set seems to be encompassed in the main seismogenic volume, calculation of static Coulomb stress changes was performed assuming different frictional behavior at the source, as commonly used to understand earthquake interactions that explain off-fault aftershock distribution and seismicity triggering. These changes that are due to the coseismic slip of the main shock are computed using the following equation:

$$\Delta \mathrm{CFF} = \Delta\tau + \mu\,(\Delta\sigma + \Delta p) \tag{1}$$

where $\Delta\tau$ is the shear stress change onto the fault plane (positive in the direction of fault slip), $\Delta\sigma$ is the fault-normal stress change (positive for increasing tensional normal stress), Δp is the pore pressure change in the rupture area, and μ is the friction coefficient, which takes values between 0.6 and 0.8 (Harris 1998; and references therein). The pore pressure change during the coseismic phase, when the porous medium is considered still under undrained conditions, according to Rice and Cleary (1976) is given by:

$$\Delta p = -B\frac{\Delta\sigma_{kk}}{3} \tag{2}$$

where B is the Skempton's coefficient ($0 \leq B<1$) and $\Delta\sigma_{kk}$ is the trace of the induced stress tensor. The undrained case is therefore considered (Beeler et al. 2000) where Δp depends upon the normal stress change on the considered fault plane.

For a planar approximation of the fault plane, the locations of the aftershocks were considered to represent points onto the same plane and the CMT solution and aftershock locations were considered together for constraining a dip of 12°. The average coseismic slip was calculated equal to 1.05 m from the moment provided from CMT solution ($M_o = 4.42 \times 10^{19}$ N m), the fault area as defined above and a rigidity equal to 33 GPa (taken as that for crustal earthquakes), equal to 0.71 m for $G = 49$ GPa (to encompass both crustal and mantle values, after Bird and Kagan 2004; Papadimitriou and Karakostas 2008) and equal to 0.44 m for $G = 80$ GPa (Toda and Stein 2013). For the coefficient of friction, we adopted values that after testing were found the most appropriate for fitting stress changes calculations and triggered seismicity (e.g., Karakostas et al. 2003, 2014; Toda et al. 2011). A coefficient of friction equal to $\mu = 0.75$ and $B = 0.5$ were considered that give an

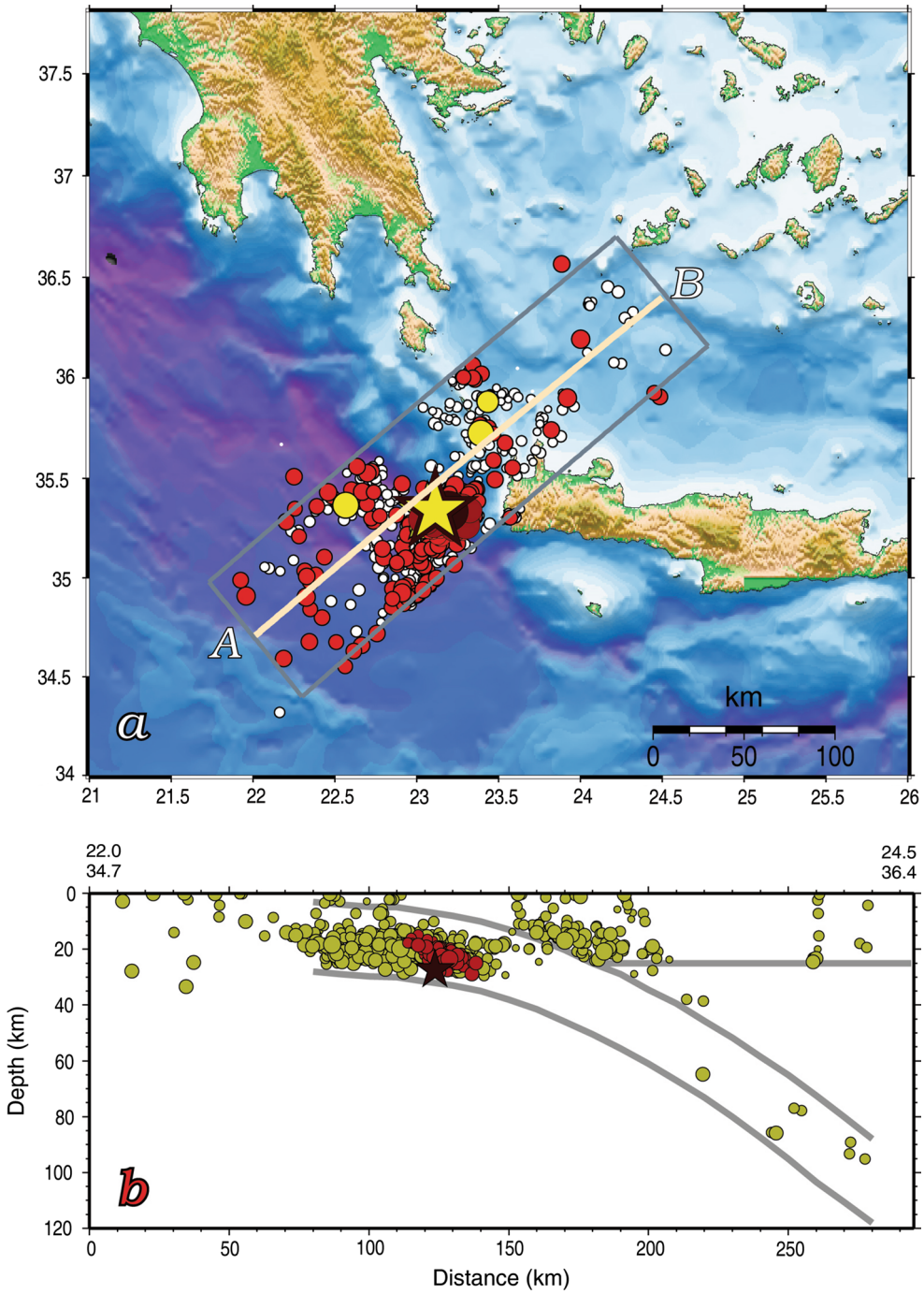

Fig. 7 **a** Map of the study area with relocated seismicity during 2011–2015 at a distance of 40 km either side of line AB. Relocation was performed with double-difference technique for all earthquakes but the ones located at the southwestern part of the area included in the rectangle, due to the small earthquake number. The *big start* denotes the main shock epicenter. *b* Cross section along the line AB with the same strike as in Fig. 6 with the 2011–2015 seismicity relocated with the double-difference technique (*in olive*) and 2013 aftershock sequence (*in red*) with the main shock location depicted with a *star*

apparent coefficient of friction $\mu' \cong 0.4$ (=0.375), which is commonly accepted as more representative (e.g., Toda et al. 2011). The Poisson's ratio was fixed to 0.25.

We also assume that the aftershocks, being all much smaller in magnitude ($1.7 \leq M \leq 4.0$) than the main shock, exhibit the same kind of faulting. Coulomb stress changes were thus calculated according to the faulting type of the main shock. Stress pattern differs substantially for the different values of rigidity, without strong evidence for off-fault seismicity triggering (Fig. 8). As suggested by Lin

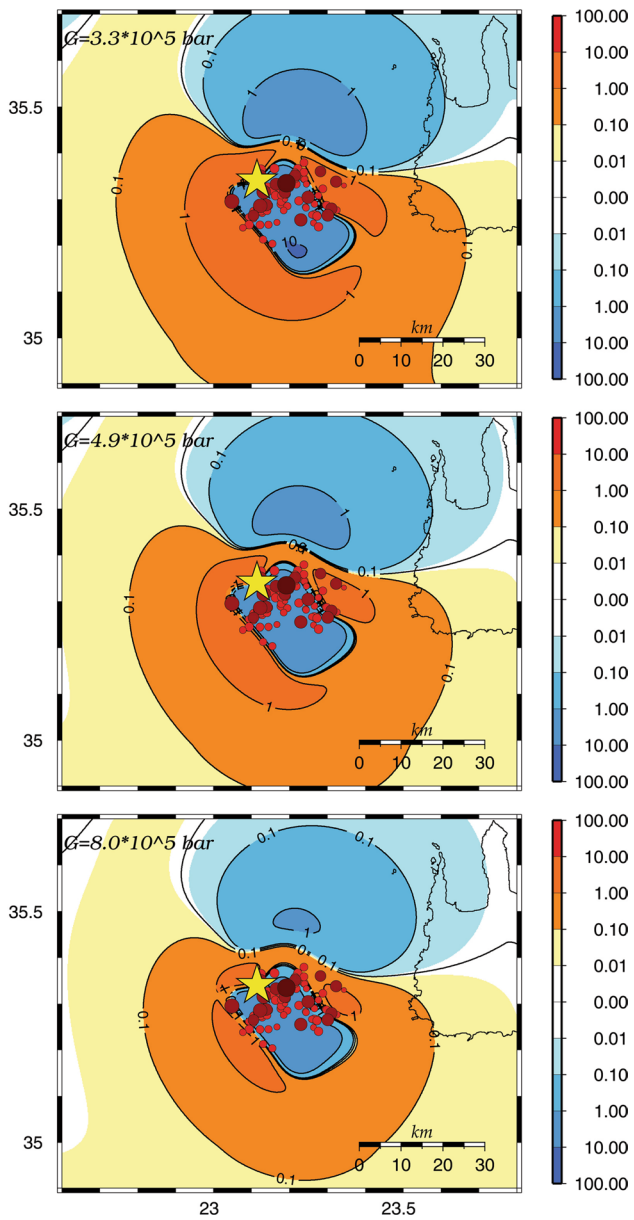

Fig. 8 Coulomb stress changes due to the coseismic slip of the main shock calculated at a depth of 25.0 km and for three different values of the shear modulus ($G = 3.3 \times 10^5$ bar, $G = 4.9 \times 10^5$ bar and $G = 8.0 \times 10^5$ bar). Changes are denoted by the *color scale* to the *right* (*in bars*) and by numbers on the contour lines. The main shock epicenter is depicted by the *star*, and the ones of aftershocks by *circles*, the color and size of which are scaled according to magnitude

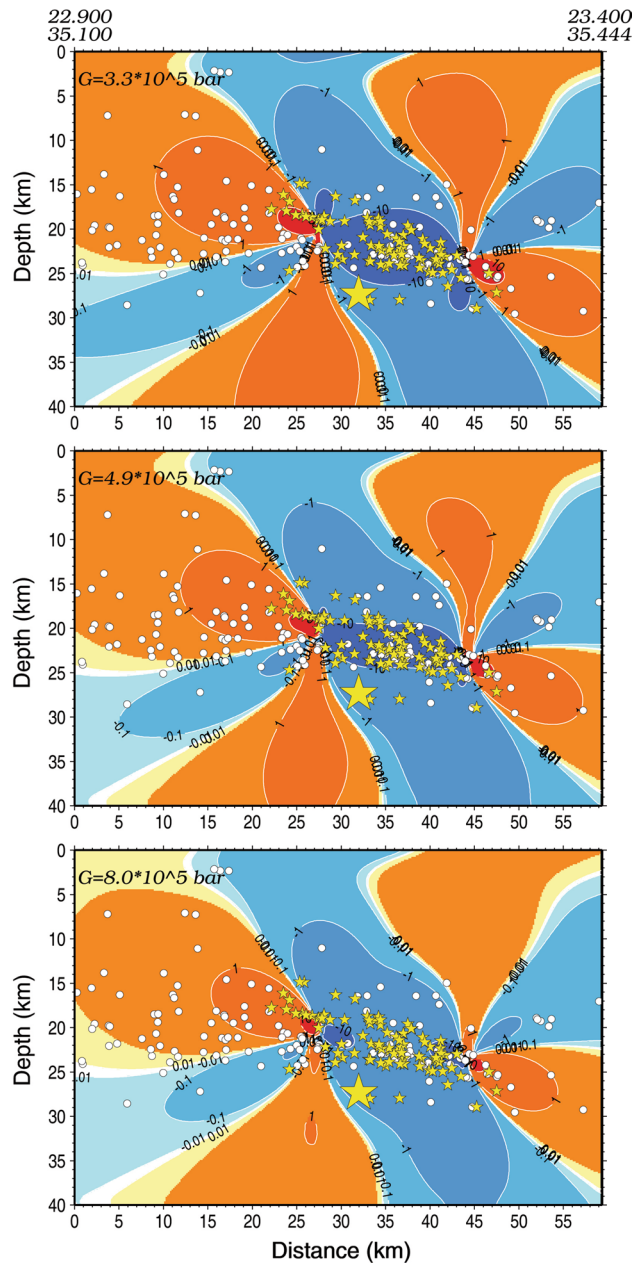

Fig. 9 Coulomb stress changes due to the coseismic slip of the main shock calculated onto the vertical plane indicating by the line SN1–SN2 in Fig. 5, and for three different values for the shear modulus ($G = 3.3 \times 10^5$ bar, $G = 4.9 \times 10^5$ bar and $G = 8.0 \times 10^5$ bar). Color scale and contouring same as in Fig. 6

and Stein (2004), stress transfer in a thrust fault is less well understood that for strike-slip and normal faults and for this reason the distribution of stress changes in the thrust faults must be analyzed three dimensionally. Calculations are for this scope repeated for a cross section and for the three rigidity values, as for the map views (Fig. 9). The vertical distribution also shows that the aftershocks (depicted by stars in Fig. 9) occurred in negative stress areas. Excluding the onto-fault aftershocks, because their locations cannot be explained in the lack of detailed slip model, the possibility for smaller faults of rather different geometry than the main shock cannot be ruled out, but since it concerns an adjacent structure, much more information is necessary for documenting this hypothesis. The seismicity taking place after the 2013 seismic excitation, that is, during 2014–2015, is also plotted (white circles in Fig. 9), which

seems to be enhanced and mainly associated with areas of positive stress changes.

Discussion and conclusions

The main scope of this study is the recognition of slab geometry and mode of deformation along the southwestern part of the Hellenic Arc, manifested by the 2013 seismic sequence, which occupied an area where no prior event had been located since at least 1900, and constituting the first aftershock sequence recorded by the modern regional seismological network. The main shock and aftershocks relocation imply that the main shock ruptured a patch of 24 km long and 17 km wide, of high and homogeneously distributed slip, perhaps representing frictional or structural homogeneity across the subduction interface. It became tantalizing to constrain the rupture dimensions because the relocated seismicity implied that the rupture began at the western part of the activated area, then the aftershocks activity expanded to east–southeast mainly and continues in the same area up to 50 days afterward. Aftershock activity is sparse around the main shock epicenter, and it is also lacking far from the main rupture area. Based on numerous investigations worldwide, in areas with densely distributed seismic monitoring stations and perfect azimuthal coverage, it appears that aftershocks which occur on or very near the main shock rupture are actually quite rare in large-slip regions; instead, aftershocks seem to occur mostly outside or peripheral to these large-slip zones (Karakostas et al. 2003, 2004, for the area of Greece; Kato and Igarashi 2012; and reference therein). The above statement in combination with the aftershock distribution implies a high-slip area around where the main shock focus is encompassing, located at the western part of the activated segment. The main shock was originated at a depth of 26 km, at the lower part of the activated fault segment, which probably signifies the depth of the seismogenic layer at this part of the slab. This thickness of the brittle crustal layer agrees perfectly with the findings of Li et al. (2003) who suggested that Moho is located at 32 and 31 km for western and southern Crete, respectively. The shallow-dipping thrust faulting implies slip at the coupled part of the slab, where compression is oblique to the subduction interface (P-axis: 211°/42°). Further downdip the existence of slab pull events is evidenced by recent occurrences (e.g., 2006 Kythira M_w6.7 intermediate depth earthquake; Nikolintaga et al. 2008).

One intriguing question is whether faulting geometry of the 2013 main shock is representative for the plate interface at this site, the southwestern part of the Hellenic Arc, accommodating the 365 AD M_w8.4 earthquake (Papadimitriou and Karakostas 2008) the largest known earthquake in the Mediterranean region. The fact that the current activity took place at the coupled part of the slab makes the current investigation important for future seismic assessment, in accordance with the concept of modeling Wadati–Benioff zone (WBZ) geometry in subduction zones (Hayes et al. 2009), focused on the shallowest part of the subducting slab where the greatest hazard from large mega thrust earthquakes exists.

Since it concerns an area of a megathrust earthquake, it became evident that fault conditions on the megathrust interface can support both seismic and aseismic rupture. Hayes et al. (2014) concluded that segments or patches of subduction zones that undergo aseismic/slow slip during interseismic periods may also support significant seismic rupture during megathrust earthquakes, extending the coseismic rupture area and increasing the maximum magnitude that could occur on those plate boundary segments. Alternatively, the strong strike-slip component of the main rupture perhaps did not highlight the predominant thrust component responsible for strain accumulation onto the interface that promotes seismogenesis. Most probably strong thrust aftershocks could not be generated, and this also explains that the strongest aftershock had magnitude just only $M = 4.0$.

To inspect possible triggering outside the main rupture either of nearby faults along strike or across the slab interface, Coulomb stress changes were calculated based on a simplified geometry of the rupture plane, which was defined from the relocated aftershocks spatial distribution, as described in a previous section. It came out that, although favored, stress transfer was not adequate to trigger nearby smaller fault patches, an observation that agrees with the stable upper part of the descending slab, as it was evidenced in the aftershock vertical distribution. Nevertheless, seismicity in a broader area was noticeably increased and found to be mainly associated with areas of positive Coulomb stress changes.

Acknowledgments The constructive comments of one anonymous reviewer and Thanassis Ganas are greatly appreciated. Gratitude is also extended to Prof. W.-C. Dullo and Prof. P. Xypolias for their editorial assistance. The stress tensors were calculated using a program written by J. Deng (Deng and Sykes 1997), based on the DIS3D code of S. Dunbar, which later improved (Erikson 1986) and the expressions of G. Converse. Some plots were made using the Generic Mapping Tools version 4.5.3 (www.soest.hawaii.edu/gmt, Wessel and Smith 1998). This work was implemented through the project entitled "Interdisciplinary Multi-Scale Research of Earthquake Physics and Seismotectonics at the Front of the Hellenic Arc (IMPACT-ARC)" in the framework of action "ARCHIMEDES III—Support of Research Teams at TEI of Crete" (MIS380353) of the Operational Program "Education and Lifelong Learning" and is co-financed by the European Union (European Social Fund) and Greek national funds. Geophysics Department Contribution 850.

Appendix

Information on all known historical earthquakes with $M \geq 7.0$ that occurred in the southern Aegean area, most of them along the Hellenic subduction zone (from Papazachos and Papazachou 2003)

Occurrence date	Occurrence time Month/date	Latitude (°N)	Longitude (°E)	Depth (km)	*M*
−227		36.400	28.400		7.5
−198	08/	36.300	28.200		7.2
−27		37.800	28.100		7.2
62		34.800	24.100		7.5
142		36.300	29.000		7.5
251	07/09	35.600	25.000	61	7.5
365	07/21	35.200	23.400		8.3
448	11/06	34.800	24.800		7.2
556	08/	36.800	27.300		7.0
796	04/	34.500	24.400		7.1
1246		35.400	23.300		7.0
1303	08/18	36.100	29.400		8.0
1366	04/30	36.800	28.600		7.2
1481	05/03	36.200	29.000		7.2
1494	07/01	35.500	23.300		7.5
1508	05/29	35.200	25.800		7.2
1513	03/28	36.100	28.200		7.2
1609	04/	36.200	29.000		7.2
1612	11/08	35.000	23.800		7.2
1630	03/09	35.000	23.700		7.3
1633	11/05	37.700	20.800		7.0
1653	02/22	37.760	27.800		7.1
1681	01/10	35.400	23.500		7.0
1702	02/25	37.700	29.100		7.0
1717		35.900	22.900		7.0
1741	01/31	36.200	29.300		7.4
1750	06/07	36.300	22.800		7.2
1754	06/15	37.800	22.500	61	7.0
1756	02/13	36.300	27.500	61	7.5
1805	07/03	35.000	24.000		7.0
1810	02/16	35.500	25.600	90	7.5
1846	03/28	35.800	25.000	90	7.2
1856	10/12	35.600	25.800	61	7.7
1862	06/21	36.900	24.400	150	7.0
1863	04/22	36.400	27.600	90	7.5
1874	11/16	36.500	27.900	61	7.0
1886	08/27	37.000	21.400		7.3
1887	07/17	35.700	25.800	100	7.2
1898	06/02	37.600	22.600	90	7.0
1899	09/20	37.820	28.250		7.0
1903	08/11	36.360	22.970	80	7.2
1911	04/04	36.500	25.500	140	7.1
1926	06/26	36.500	27.500	100	7.6
1926	08/30	36.500	23.300	100	7.2
1927	07/01	36.780	22.260		7.1
1935	02/25	35.900	25.200	100	7.0
1947	10/06	36.960	21.680		7.0
1948	02/09	35.700	27.000		7.1
1952	12/17	34.400	24.500		7.0
1956	07/09	36.640	25.960		7.5
1957	04/25	36.500	28.600		7.2

References

Beeler NM, Simpson RW, Hickman SH, Lockner DA (2000) Pore fluid pressure, apparent friction and Coulomb failure. J Geophys Res 105:25533–25542

Bird P, Kagan YY (2004) Plate-tectonic analysis of shallow seismicity: apparent boundary width, beta, corner magnitude, coupled lithosphere thickness, and coupling in seven tectonic settings. Bull Seismol Soc Am 94:2380–2399

Deng J, Sykes L (1997) Evolution of the stress field in Southern California and triggering of moderate size earthquakes: a 200-year perspective. J Geophys Res 102:9859–9886

Erikson L (1986) User's manual for DIS3D: a three-dimensional dislocation program with applications to faulting in the Earth. Master's Thesis, Stanford University, Stanford, California, pp 167

Ganas A, Parsons T (2009) Three-dimensional model of Hellenic Arc deformation and origin of the Cretan uplift. J Geophys Res. doi:10.1029/2008JB005599

Govers R, Wortel MJR (2005) Lithosphere tearing at STEP faults: response to edges of subduction zones. Earth Planet Sci Lett 236:505–523

Harris RA (1998) Introduction to special section: stress triggers, stress shadows, and implications for seismic hazard. J Geophys Res 103:24347–24358

Hatzfeld D, Pedottti G, Hatzidimitriou P, Makropoulos K (1990) The strain pattern in the western Hellenic Arc deduced from a microearthquake survey. Geophys J Int 101:181–202

Hayes GP, Wald DJ, Keranen K (2009) Advancing techniques to constrain the geometry of the seismic rupture plane on subduction interfaces a priori: higher-order functional fits. Geochem Geophys Geosyst. doi:10.1029/2009GC002633

Hayes GP, Furlong KP, Benz HM, Herman MW (2014) Triggered aseismic slip adjacent to the 6 February 2013 Mw 8.0 Santa Cruz Islands megathrust earthquake. Earth Planet Sci Lett 388:265–272

Hloupis G, Papadopoulos I, Makris JP, Vallianatos F (2013) The south Aegean seismological network—HSNC. Adv Geosci 34:15–21

Karakostas VG, Papadimitriou EE, Karakaisis GF, Papazachos CB, Scordilis EM, Vargemezis G, Aidona E (2003) The 2001 Skyros, Northern Aegean, Greece, earthquake sequence: off–fault aftershocks, tectonic implications, and seismicity triggering. Geophys Res Lett. doi:10.1029/2002GL15814

Karakostas VG, Papadimitriou EE, Papazachos CB (2004) Properties of the 2003 Lefkada, Ionian Islands, Greece, earthquake seismic sequence and seismicity triggering. Bull Seismol Soc Am 94:1976–1981

Karakostas VG, Papadimitriou EE, Gospodinov D (2014) Modeling the 2013 North Aegean (Greece) seismic sequence: geometrical and frictional constraints, and aftershock probabilities. Geophys J Int 197:525–541. doi:10.1093/gji/ggt523

Kato A, Igarashi T (2012) Regional extent of the large coseismic slip zone of the 2011 M_w9.0 Tohoku-Oki earthquake delineated by on-fault aftershocks. Geophys Res Lett. doi:10.1029/2012GL052220

Kiratzi AA, Langston C (1989) Estimation of earthquake source parameters of the May 4, 1972 event of the Hellenic Arc by the inversion of waveform data. Phys Earth Planet Inter 57:225–232

Klein FW (2000) User's Guide to HYPOINVERSE–2000, a Fortran program to solve earthquake locations and magnitudes. U.S. Geological Survey Open File Report 02–171 Version 1.0

Li X, Bock G, Vafidis A, Kind R, Harjes H-P, Hanka W, Wylegalla K, van der Meijde M, Yuan X (2003) Receiver function study of the Hellenic subduction zone: imaging crustal thickness variations and the oceanic Moho of the descending African lithosphere. Geophys J Int 155:733–748

Lin J, Stein RS (2004) Stress triggering in thrust and subduction earthquakes and stress interaction between the southern San Andreas and nearby thrust and strike-slip faults. J Geophys Res. doi:10.1029/2003JB002607

McClusky S, Balassanian S, Barka A, Demir C, Georgiev I, Hamburger M, Hurst K, Kahle H, Kastens K, Kekelidze G, King R, Kotzev V, Lenk O, Mahmoud S, Mishin A, Nadariya M, Ouzounis A, Paradisis D, Peter Y, Prilepi M, Reilinger R, Sanli I, Seeger H, Tealeb A, Toksoz MN, Veis G (2000) GPS constraints on crustal movements and deformations in the Eastern Mediterranean (1988–1997): implications for plate dynamics. J Geophys Res 105:5695–5719

Meier T, Rische M, Endrun B, Vafidis A, Harjes H-P (2004) Seismicity of the Hellenic subduction zone in the area of western and central Crete observed by temporary local seismic networks. Tectonophysics 383:149–169

Nikolintaga I, Karakostas V, Papadimitriou E, Vallianatos F (2008) The 2006 Kythira (Greece), M_w6.7 slab-pull event: tectonic implications and the geometry of the Hellenic Wadati-Benioff zone. Ann Geophys 51:823–837

Paige CC, Saunders MA (1982) LSQR: sparse linear equations and least squares problems. ACM Trans Math Softw 8(2):195–209

Papadimitriou E (1993) Focal mechanism along the convex side of the Hellenic Arc. Boll Geof Teor Appl XXXV:401–426

Papadimitriou E, Karakostas V (2005) Faulting geometry and seismic coupling of the southwest part of the Hellenic subduction zone. Abstract in 33rd IASPEI General Assembly, Santiago, Chile, 2–8 October 2005

Papadimitriou EE, Karakostas VG (2008) Rupture model of the great AD 365 Crete earthquake in the southwestern part of the Hellenic Arc. Acta Geophys 56:293–312

Papazachos BC, Comninakis PE (1971) Geophysical and tectonic features of the Aegean Arc. J Geophys Res 76:8517–8533

Papazachos BC, Papazachou C (2003) The earthquakes of Greece. Ziti Publication, Thessaloniki, p 317

Papazachos BC, Papadimitriou EE, Kiratzi AA, Papazachos CB, Louvari EK (1998) Fault plane solutions in the Aegean Sea and the surrounding area and their tectonic implication. Boll Geof Teor Appl 39:199–218

Papazachos BC, Karakostas BG, Papazachos CB, Scordilis EM (2000) The geometry of the Benioff zone and lithospheric kinematics in the Hellenic Arc. Tectonophysics 319:275–300

Pirazzoli PA, Laborel J, Stiros SC (1996) Earthquake clustering in the eastern Mediterranean during historical times. J Geophys Res 101:6083–6097

Reilinger RE, McClusky SC, Paradissis D, Ergintav S, Vemant P (2010) Geodetic constraints on the tectonic evolution of the Aegean region and strain accumulation along the Hellenic subduction zone. Tectonophysics 488:22–30

Rice J, Cleary M (1976) Some basic stress diffusion solutions for fluid saturated elastic porous media with compressible constituents. Rev Geophys 14:227–241

Schaff DP, Waldhauser F (2005) Waveform cross-correlation-based differential travel-time measurements at the northern California seismic network. Bull Seismol Soc Am 95:2446–2461

Schaff DP, Bokelmann GHR, Ellsworth WL, Zanzerkia E, Waldhauser F, Beroza G (2004) Optimizing correlation techniques for improved earthquake location. Bull Seismol Soc Am 94:705–721

Scordilis EM, Karakaisis GF, Karakostas BG, Panagiotopoulos DG, Comninakis PE, Papazachos BC (1985) Evidence for transform faulting in the Ionian Sea: the Cephalonia Island earthquake sequence. Pure Appl Geophys 123:388–397

Taymaz T, Jackson J, Westaway R (1990) Earthquake mechanisms in the Hellenic trench near Crete. Geophys J Int 102:695–731

Toda S, Stein R (2013) The 2011 M = 9.0 Tohoku oki earthquake more than doubled the probability of large shocks beneath Tokyo. Geophys Res Lett 40:2562–2566. doi:10.1002/grl.50524

Toda S, Lin J, Stein R (2011) Using the 2011 M = 9.0 Tohoku earthquake to test the Coulomb stress triggering hypothesis and to calculate faults brought closer to failure. Earth Planets Space 63:725–730

Wadati K (1933) On the travel time of earthquake waves, Part II. Geophys Mag 7:101–111

Waldhauser F (2001) HypoDD—a program to compute double-difference hypocenter locations, US Geological Survey Open File Report, pp 01–113

Waldhauser F, Ellsworth WL (2000) A double-difference earthquake location algorithm: method and application to the Northern Hayward Fault, California. Bull Seismol Soc Am 90:1353–1368

Wessel P, Smith WHF (1998) New, improved version of the Generic Mapping Tools Released. EOS Trans AGU 79:579